1   Revision 2

2

3   # Metastable structural transformations and pressure-induced amorphization in natural (Mg,Fe)$_2$SiO$_4$ olivine

4   ## under static compression: A Raman spectroscopic study.

5

6

7   David Santamaria-Perez[1,2], Andrew Thomson[1], Alfredo Segura[2], Julio Pellicer-Torres[2], Francisco J. Manjon[3] , Furio Corà[4],

8   Kit McColl[4], Mark Wilson[5], David Dobson[1], Paul F. McMillan[4,*]

9   [1] *Earth Sciences Department, University College London, London (UK)*

10   [2] *Departamento de Física Aplicada-ICMUV, Universidad de Valencia, Valencia (Spain)*

11   [3] *Instituto de Diseño para la Fabricación y Producción Automatizada, Universitat Politècnica de València, Valencia (Spain)*

12   [4] *Department of Chemistry, Christopher Ingold Laboratory, University College London, London WC1H 0AJ (UK)*

13   [5] *Department of Chemistry,Physical and Theoretical Chemistry Laboratory, University of Oxford, South Parks Road, Oxford,*

14   *OX1 3QZ (UK)*

15

16   ## Abstract

17   Raman spectroscopic data were obtained for natural (Mg,Fe)$_2$SiO$_4$ samples during compression to 57 GPa. Single crystals of
18   San Carlos olivine compressed to above 41 GPa using He as a pressure-transmitting medium showed appearance of a new
19   "defect" peak in the 820-840 cm^{-1} region associated with SiOSi linkages appearing between adjacent SiO$_4^{4-}$ tetrahedra to
20   result in 5- or 6-fold coordinated silicate species. Appearance of this local structural defect is accompanied by observation of
21   broad background features that typically signal the presence of amorphous material formed by pressure-induced
22   amorphization (PIA). The defect formation and PIA phenomena represent responses of the crystalline material compressed
23   metastably to beyond its stability range at low temperature. The structural changes occur at lower pressure than the
24   metastable crystalline transitions of end-member Mg$_2$SiO$_4$ forsterite (Fo-I) into new Fo-II and Fo-III phases reported recently.
25   We complemented our experimental study using density functional theory (DFT) calculations and anisotropic ion molecular
26   dynamics (AIMD) simulations to investigate the Raman spectra and vibrational density of states (VDOS) of metastably
27   compressed Mg$_2$SiO$_4$ olivine, Fo-II and Fo-III, and quenched melts at high and low pressures. By 54 GPa all sharp crystalline
28   peaks had disappeared from our observed Raman spectra indicating completion of the PIA process. The resulting
29   amorphous (Mg,Fe)$_2$SiO$_4$ spectrum contains Si-O stretching bands at lower wavenumber than expected for SiO$_4^{4-}$ species
30   indicating higher coordination of the silicate units. The amorphous spectrum was maintained on decompression to ambient
31   conditions but showed evidence for reappearance of tetrahedrally-coordinated units below approximately 30 GPa.
32   Experiments designed to produce highly non-hydrostatic compression conditions for polycrystalline olivine showed similar
33   appearance of the defect feature and broad amorphous features between 43-44 GPa. Both increased in intensity as the
34   sample was left at pressure overnight but these both disappeared during decompression below 17 GPa, with recovery of a
35   polycrystalline olivine Raman signature. A hydrated San Carlos olivine sample containing 75-150 ppm OH was also
36   investigated. Significant broadening of the SiO$_4^{4-}$ stretching peaks was observed above 43 GPa but without immediate
37   appearance of the defect or broad amorphous features on initial compression. However both of these characteristics
38   emerged after leaving the sample at 47 GPa overnight, followed by complete amorphization upon subsequent pressurization
39   to 54 GPa. During decompression the high density amorphous material was retained to 3 GPa, but on final pressure release
40   a spectrum similar to thermally quenched low pressure olivine glass containing isolated SiO$_4^{4-}$ groups was obtained. Leaving
41   this sample overnight resulted in recrystallization of olivine. Our experimental data provide new insights into the metastable
42   structural transformations and relaxation behavior of olivine samples including material recovered from meteorites and
43   laboratory shock experiments.

44

45   **Keywords**: San Carlos olivine, Raman spectroscopy, metastable phase transition, defect formation, amorphization, high
46   density silicate glass

47   * Corresponding author email: p.f.mcmillan@ucl.ac.uk

1

48

Introduction

50   Olivine (α-(Mg,Fe)$_2$SiO$_4$) is the dominant mineral of the Earth′s upper mantle and is present within chondritic

51   meteorites as well as a wide range of other extra-terrestrial environments (see Finkelstein et al 2014 for a

52   summary of literature). It is important to understand the stable and metastable structural transformations that occur

53   for this important mineral phase as it experiences static and dynamic compression followed by recovery to ambient

54   conditions. Equilibrium phase relations within the Mg$_2$SiO$_4$-Fe$_2$SiO$_4$ system are well established from high pressure

55   (P) - high temperature (T) experiments. α-Mg$_2$SiO$_4$ (forsterite; Fo) transforms first into spinelloid β-Mg$_2$SiO$_4$

56   (wadsleyite) and then spinel-structured γ-Mg$_2$SiO$_4$ (ringwoodite) phases at between P = 12 - 22 GPa depending

57   upon the temperature, before chemically dissociating into MgSiO$_3$ perovskite (bridgmanite) + MgO above

58   approximately 25 GPa. The α-Fe$_2$SiO$_4$ end-member (fayalite, Fa) transforms directly into its spinel-structured γ-

59   phase at P = 6 - 7 GPa. Changes in density, elastic properties and mineral rheology associated with the α-β-γ

60   phase transitions in the Mg$_2$SiO$_4$ - Fe$_2$SiO$_4$ system are used to interpret the seismic discontinuities observed within

61   the Earth's upper mantle and transition zone (Ringwood 1991). High-P,T transformations of Fo-Fa olivine solid

62   solutions also give rise to the wadsleyite and ringwoodite phases found among chondritic meteorite samples.

63   Metastable structural transformations and phase changes are encountered as (Mg,Fe)$_2$SiO$_4$ olivine is

64   pressurized beyond its normal stability limits at low temperature or on rapid timescales. Mao and Bell (1972)

65   measured electrical conductivity and optical absorption spectra of fayalite up to 30 GPa and reported a large

66   conductivity increase and a red shift in the optical absorption edge. Shulien et al (1978) recorded a similar

67   conductivity increase during shock experiments for natural Fe-rich dunite. Mashimo et al (1980) subjected single

68   crystals of synthetic fayalite to shock compression between 19.5-56 GPa and confirmed the large increase in

69   electrical conductivity. They noted a change in Hugoniot slope at around 30 GPa suggesting the presence of a

70   phase transformation. Williams et al (1990) obtained X-ray diffraction, IR and visible absorption spectroscopy and

71   electrical conductivity data for Fe$_2$SiO$_4$ olivine in the diamond anvil cell (DAC). The band gap closure and

72 conductivity increase were interpreted as due to increased interactions and possible electronic disproportionation

73 between the Fe^{2+} ions. Pressure induced amorphization (PIA) was proposed to occur above 39 GPa associated

74 with an increase in the average local coordination of silicate units. However the coordination change was not

75 retained during decompression to ambient conditions. X-ray diffraction results obtained by Richard and Richet

76 (1990) in the DAC likewise indicated amorphization of metastably compressed fayalite at 35 GPa. They found that

77 the amorphous phase could be recovered to room pressure, but that the silicate units reverted to fourfold

78 coordination during decompression.

79   The occurrence of PIA among Mg-rich olivine samples is less well documented. Jeanloz et al (1977)

80 reported amorphous zones occurring within a natural $(Mg_{0.88}Fe_{0.12})_2SiO_4$ crystal shocked in the laboratory to > 56

81 GPa. However, Jeanloz (1980) later examined single crystal samples of $(Mg,Fe)_2SiO_4$ olivines recovered following

82 shock compression to between 25 - 70 GPa using TEM and IR spectroscopy. He concluded that the amorphous

83 zones observed previously corresponded to localized regions of intense strain that constituted no more than a few

84 percent of any sample. Heymann and Cellucci (1988) examined a shocked sample of natural dunite using Raman

85 spectroscopy and observed a broad feature at 1100 cm^{-1} that they interpreted as due to olivine glass formed

86 during the shock experiment. However, during a later study of a suite of shocked chondrite samples Heymann

87 (1990) concluded that the feature was mainly due to luminescence effects. Guyot and Reynard (1992) subjected

88 San Carlos olivine $(Mg,Fe)_2SiO_4$ samples to high-P,T treatment at temperatures below 700°C in a laser-heated

89 DAC. They observed that samples recovered from > 70 GPa appeared amorphous to examination by transmission

90 electron microscopy (TEM) and electron diffraction, but materials recovered from lower pressure (30-70 GPa)

91 showed the presence of intermediate crystalline phases with a hexagonally-close packed (hcp) lattice. Andrault *et*

92 *al.* (1995) carried out *in situ* energy-dispersive X-ray diffraction at up to 50 - 69 GPa for olivines along the Mg_2SiO_4

93 - Fe_2SiO_4 join. They observed PIA occurring for fayalite as previously reported, but observed that although broad

94 amorphous features were observed to occur at increasingly higher pressures as the Fo content increased, some

95 crystalline diffraction remained for all the other samples to the highest pressures examined. They concluded that

96 PIA occurred as a continuous transformation process within parts of the crystalline samples, and that the

97 metastable transformations could be associated with a kinetically frustrated structural transition to wadsleyeite (β-

98 Mg_2SiO_4) or another spinelloid type structure.

99 Raman spectroscopic investigations of $(Mg,Fe)_2SiO_4$ olivines recovered from natural meteorites as well as

100 laboratory shocked samples have revealed additional peaks in the 600-800 cm^{-1} range that are not predicted to

101 occur for the olivine structure (Farrell-Turner *et al.*, 2005; Van de Moortèle *et al.*, 2007). A similar band observed to

102 appear in the Raman spectra of polycrystalline α-Mg_2SiO_4 compressed to above 31 GPa was assigned to the

103 formation of local "defects" associated with Si-O-Si linkages involving highly coordinated SiO_n (e.g., n = 5,6)

104 species (Durben *et al.* 1993). An analogous feature was also noted to appear for β-Mg_2SiO_4 samples heated

105 metastably at ambient pressure (McMillan et al., 1991). Van de Moortele *et al.* (2007) combined their Raman and

106 TEM observations of unusual dark-colored veins of shocked olivine in two Martian meteorites (NWA 2737 and

107 NWA 1950) with MD simulation results to suggest possible formation of a metastable $(Mg,Fe)_2SiO_4$ phase from

108 shock compression of Mg-rich olivine to between 35-50 GPa. However the proposed ζ-$(Mg,Fe)_2SiO_4$ structure did

109 not contain any highly-coordinated silicate species.

110 Finkelstein et al (2014) carried out a detailed structural investigation of α-Mg_2SiO_4 using single crystal X-

111 ray diffraction during quasi-hydrostatic compression in He to 90 GPa. They observed that the forsterite structure

112 remained intact up to 48 GPa and they identified phase transitions occurring within the metastably compressed

113 material at 50 and 58 GPa to two new polymorphs labelled forsterite (Fo-) II and -III, respectively. These structures

114 and metastable phase transitions were identified by *ab initio* evolutionary crystal structure prediction and

115 metadynamics simulations carried out using density functional theory (DFT). The new phases contain SiO_4 and

116 SiO_6 units connected by Si-O-Si linkages formed between the previously isolated SiO_4^{4-} tetrahedra, and 5-

117 coordinated SiO_5 species were also suggested to appear during the metastable structural transformation process

118 from olivine.

119   In the present work we report Raman spectroscopic results for single crystal and polycrystalline samples

120   of natural San Carlos $(Mg,Fe)_2SiO_4$ olivine compressed under quasi- and non-hydrostatic conditions to 57 GPa.

121   We also completed density functional theory (DFT) calculations on the Mg end-member olivine (Mg_2SiO_4,

122   forsterite) using the CRYSTAL14 code (Dovesi et al., 2014) to help interpret the experimental data. Our

123   compression results differ from those of Finkelstein et al. (2014) in that we observe appearance of "defect"

124   features associated with formation of SiOSi linkages and highly coordinated SiO_5 or SiO_6 species above 42 GPa

125   within the single crystalline sample, along with PIA that is completed by 54 GPa. The amorphous solid is

126   recovered to ambient conditions and it clearly contains highly coordinated silicate species and is different from

127   olivine glass produced by quenching from the melt phase. Slightly different compression and decompression

128   behavior is observed for polycrystalline and OH-containing samples. We discuss these observations in terms of

129   metastable transformations occurring for $(Mg,Fe)_2SiO_4$ olivine materials and highlight their importance for

130   analyzing and interpreting materials recovered from meteorite samples as well as static and dynamic compression

131   experiments.

132   **Experimental**

133   Our crystals were extracted from the same xenolith as the material studied by Demouchy and Mackwell (2006).

134   Electron microprobe analyses gave the composition $(Mg_{1.81}Fe_{0.18}Ni_{0.01})_2SiO_4$ typical for San Carlos olivine (Fournelle,

135   2011). The OH content was below the detection limit for Fourier transform infrared (FTIR) spectroscopy (<1 ppm

136   H_2O). For our first series of room temperature pressurization experiments a polished single-crystal of approximate

137   dimensions 14x22x8 μm^3 was oriented with its b axis perpendicular to the diamond culet and placed in a 80 μm

138   hole of a Re gasket pre-indented to 32 μm. Pressurization and decompression studies were carried out using a

139   He gas membrane-drive diamond anvil cell (DAC) (Almax-Easylab) with bevelled diamond anvils (150 μm outer

140   culet). Pressure was determined by ruby fluorescence. Helium was introduced into the cell by high-pressure gas

141   loading to act as a hydrostatic pressure-transmitting medium (PTM) (Klotz et al. 2009).

142   A second series of experiments was designed to investigate the compression behavior of olivine under

143   non-hydrostatic conditions. A polycrystalline material was produced by grinding the crystals in an agate mortar to

144   produce micron-sized grains. The resulting powder was then pressed into a pellet and loaded into the cell using

145   Ne as PTM. Although Ne solidifies at 4.8 GPa it only leads to obvious signs of non-hydrostatic broadening in the

146   ruby R1 fluorescence line above 15 GPa (Klotz et al. 2009). However, a range of highly non-hydrostatic

147   pressurization conditions occurs throughout the polycrystalline pressed powder sample at all pressures as a result

148   of intergrain contacts that provide high energy sites to initiate phase changes.

149   In a third experiment the effect of incorporated OH on the compression behavior of $(Mg,Fe)_2SiO_4$ olivine

150   was investigated. OH-enriched olivine was prepared by treating San Carlos crystals ground to an initial grain size

151   <50 μm at ~7 GPa and 1273 K in a multi anvil device for 43 hours. The olivine powder was packed into a graphite

152   sleeve, that was then arc-welded inside a Pt capsule. A 1.4:1 by weight talc:brucite mixture was loaded in one end

153   of the Pt capsule. This dehydrated at run conditions to produce forsterite + enstatite + H_2O thus providing a source

154   of H_2O as well as buffering a_{SiO2} during the experiment. Pressure within the multi anvil apparatus was estimated to

155   within ±1 GPa. The recovered Pt capsule released free water upon piercing and the grain size of the initial San

156   Carlos olivine had increased to several hundred μm, consistent with the sample being held under water saturated

157   conditions during the high-P,T experiment. Unpolarized FTIR spectra of recovered crystals indicated a water

158   content between 75 - 150 ppm (Withers et al., 2012). This value is similar to H_2O contents observed for samples

159   hydrated in the presence of H_2O-CO_2 fluids (Yang et al., 2014), but is lower than the maximum OH solubility in

160   olivine at similar P,T conditions in equilibrium with pure H_2O (Kohlstedt et al., 1996). A fragment of the OH-

161   saturated olivine crystal approximately 20x20x10 μm in dimensions was loaded into the DAC and compressed

162   using He as PTM.

163   Raman spectra were measured in backscattering geometry with resolution <2 cm^{-1} using home-built and

164   commercial instruments in London (UCL) and in Valencia at up to 58 GPa. The UCL instrument was built around

165   an Acton 300 spectrometer and liquid N_2-cooled back-illuminated Si CCD detector (Princeton Instruments) using

6

166   Kaiser holographic supernotch filters to discriminate between incident laser and Raman scattered light (Soignard

167   and McMillan 2004). Spectra were obtained using 514.5 or 488 nm lines from an Ar^+ laser focused on the sample

168   using a Mitutoyo 50x long working distance (LWD) objective. In Valencia spectra were obtained using (i) a

169   LabRAM HR UV microspectrometer coupled to a Peltier-cooled CCD detector. The 532 nm line of a solid state

170   laser was focused on the sample using a 50x LWD objective and light was dispersed on to the detector with a

171   1200 gr/mm grating;   (ii) a home-built microscopic confocal system using 488 nm Ar^+ laser excitation and a

172   Semrock edge filter to discriminate against elastically scattered light. The Raman signal was dispersed *via* a

173   Jobin-Yvon TRH 1000 spectrometer (1200 gr/mm grating) on to a thermoelectric-cooled multichannel Synapse

174   CCD detector. Wavenumbers of all Raman instruments and experiments were calibrated using laser plasma lines

175   and a Ne lamp.

176   Density Functional Theory (DFT) calculations on the Mg end-member olivine (Mg_2SiO_4, forsterite) were

177   performed using the CRYSTAL14 code (Dovesi et al., 2014) using the B3LYP hybrid exchange functional and the

178   basis set from Noel et al. (2006). Structures of the forsterite-I, -II and -III phases at different volumes were taken

179   from Finkelstein et al (2014), followed by constant volume geometry optimizations before calculation of their zone-

180   centre Raman spectra. The Fo-III phase at the 58.2 GPa volume yielded imaginary phonons in the $Cmc2_1$ space

181   group reported by Finkelstein et al (2014). The crystallographic unit cell (4 formula units) was reoptimized without

182   symmetry, revealing small symmetry breaking atomic displacements that result in the structure remaining within

183   the P1 space group. Raman intensities were calculated using the CPKS method discussed in Maschio et al.

184   (2013a, b). The data are presented as orientationally and polarization averaged powder spectra appropriate for the

185   180° back-scattering geometry used experimentally (Prosandeev et al., 2005).

186   Molecular Dynamics (MD) simulations were carried out to further investigate the vibrational properties of

187   the metastably compressed phases. We used a similar protocol to that described in our previous study of another

188   metastable phase ("ζ-Mg_2SiO_4") predicted to form from olivine during dynamic compression (Van de Moortèle et

189   al, 2007). The calculations were carried out using an Anisotropic Ion Model (AIM) (Aguado et al., 2003), in which

190   induced ion moments and short-range size and shape deformations of O^{2-} parametrized *via* high-level electronic

191   structure calculations (Jahn and Madden, 2007) were included to quadrupolar level. The simulation contained 672

192   ions under constant P conditions with variable volume and cell dimensions at T=300 K. The vibrational densities of

193   states (VDOS) for the compressed structures were calculated by extracting 10 configurations at each pressure

194   with each time-separated by ~100ps. The Hessian matrix with elements $H_{i\mu,jv} = \dfrac{1}{m}\dfrac{\partial^2 U}{\partial r_{i,\alpha}\partial r_{j,\beta}}$ (*U* is the total

195   system energy for a given configuration $\{R^N\} = \{r_1, r_2, ..., r_N\}$) was calculated numerically and diagonalized to

196   obtain the VDOS.

197

198   **Results**

199   Mg_2SiO_4 olivine has an orthorhombic unit cell, space group *Pbnm*, containing slightly distorted (SiO_4) tetrahedra

200   along with two types of (MgO_6) octahedra (M1 and M2 sites) (Birle *et al.*, 1968). With Z=4 formula units in the

201   primitive unit cell, symmetry analysis predicts 84 vibrational modes at the Brillouin zone center. Of these, 36 are

202   Raman active: Γ_{Raman} = 11 A_g + 11 B_{1g} + 7 B_{2g} + 7 B_{3g} that have been assigned to their respective atomic

203   displacement patterns from polarized single-crystal studies and isotopic exchange experiments along with

204   empirical force field, ionic model and *ab initio* density functional theory (DFT) calculations (Servoin and Piriou,

205   1973; Pâques-Ledent and Tarte, 1973; Iishi, 1978; Price et al., 1987; Chopelas, 1991; Kolesov and Geiger, 2004;

206   Noel et al., 2006). The principal Raman peaks are the Si-O stretching modes derived from coupled vibrations of

207   the SiO_4^{4-} tetrahedra that occur between 800-1000 cm^{-1} at ambient pressure (Fig. 1). Studies of single crystalline

208   samples show changes in relative peak intensities as a function of orientation and polarization conditions (Servoin

209   and Piriou, 1973; Iishi, 1978; Chopelas, 1991; Kolesov and Geiger, 2004). In our experiments we did not collect

210   polarized data but instead oriented our sample to ensure that all major peaks were represented in the spectra. The

211   pattern of relative peak intensities resembled the *cc* data of Kolesov and Geiger (2004) (A_g modes) for a $Fo_{90}Fa_{10}$

212   sample, with the addition of B_{3g} and B_{2g} peaks (Fig. 1). The use of a membrane-driven DAC that remained

8

213   mounted in the beam while changing pressure allowed us to maintain the sample orientation throughout each

214   series of experiments.

215   In addition to Raman scattering, olivine vibrational spectra have also been studied extensively by FTIR

216   and inelastic neutron scattering (INS) spectroscopy, as well as by ion dynamics simulations and first principles

217   vibrational studies, to reveal the distribution of modes occuring throughout the Brillouin zone (Servoin and Piriou,

218   1973; Hofmeister, 1987, 1997; Rao et $al.$, 1988; Price et $al.$, 1987; Ghose et al 1991; Noel et al., 2006). The

219   modes observed are distributed according to the following groupings: ν_1 and ν_3 internal Si-O stretching of the

220   SiO_4^{4-} tetrahedra in the 820 - 980 cm^{-1} range; SiO_4^{4-} ν_2 and ν_4 bending between 420 - 650 cm^{-1}, and librational

221   modes involving Mg^{2+} cations and SiO_4 units below 470 cm^{-1}. Of particular importance for interpretation of our data

222   is that no Raman peaks, or indeed any phonons propagating throughout the Brillouin zone, occur in the range 650

223   - 820 cm^{-1}, between the tetrahedral bending and stretching modes.

224   We obtained Raman spectra of our single-crystalline sample of San Carlos olivine compressed quasi-

225   hydrostatically in He at up to 57.1 GPa (Fig. 1). The data exhibit slight peak broadening above 11 GPa leading to

226   loss of definition among the high frequency modes, and the A_g mode in the 600-680 cm^{-1} region, that is derived

227   from ν_2 deformation of the SiO_4 units, becomes more prominent above 15.7 GPa. Our DFT calculations for

228   Mg_2SiO_4 olivine based on fully isotropic averages of the derived polarizability tensor elements (Noel et al., 2006)

229   show a similar intensification of this peak (Fig. 2) so that the effect must be due to changes in vibrational coupling

230   among modes of the same symmetry (Piriou and McMillan, 1983). Both the observed and calculated peak

231   frequencies ($d\nu_i/dP$) show a regular variation with pressure, in good agreement with previous studies (Chopelas,

232   1990, 1991) (Fig. 3). The >200 cm^{-1} separation between the internal SiO_4^{4-} stretching and bending modes is

233   maintained throughout the pressure range.

234   At 41.7 GPa a new peak appears in the experimental data within the previously blank region between the

235   SiO_4 stretching and bending vibrations. This peak first appears at 820 cm^{-1} and shifts to 840 cm^{-1} by 50 GPa (Fig.

236 1). A similar peak was noted to appear in the same pressure range In a previous Raman study of polycrystalline

237 α-Mg_2SiO_4 compressed in Ar to 50 GPa (Durben *et al.*, 1993). As already noted, no vibrational features are

238 expected to occur in this intermediate range between the SiO_4 stretching and bending vibrations for the olivine

239 structure (Rao *et al.*, 1988; Price *et al.*, 1987; Ghose et al 1991; Noel et al., 2006) and none appear in our DFT

240 calculations for the compressed Mg_2SiO_4 forsterite phase (Fig. 2). Durben *et al.* (1993) proposed that the new

241 peak might indicate the formation of SiOSi linkages between adjacent SiO_4^{4-} tetrahedra resulting in the

242 appearance of highly coordinated species (e.g., SiO_5 or SiO_6 units) that could be present as localized defects

243 within the structure. Examination of the atomic displacement patterns for the vibrational modes of the Fo-II and Fo-

244 III structures allow us to refine that interpretation. In Fo-II we have both SiO_4 and SiO_6 units connected by an

245 SiOSi linkage. The peak at 895 cm^{-1} corresponds to an Si-O stretching vibration of the octahedral units

246 concentrated on the non-bridging oxygens bonded to Mg^{2+} cations. The SiOSi stretching vibration of the oxygen

247 linking the SiO_4 and SiO_6 groups appears at 1083 cm^{-1}, whereas the remaining high frequency modes at 1009,

248 1108 and 1169 cm^{-1} are mainly SiO_4 stretching vibrations involving the non-bridging oxygens. In Fo-III, all Si atoms

249 are 6-coordinated, but there is one very short Si-O bond (1.64 Å), one medium (1.70 Å) and 4 long (1.77 Å). The

250 main peaks are: 926 cm^{-1} : stretching of the long Si-O bond, connected to 4 Mg^{2+} cations; 1025 cm^{-1} : stretching of

251 the short Si-O bond, connected to 3 Mg^{2+} cations; 986 cm^{-1} : stretching of the SiOSi linkage between adjacent

252 SiO_6 units. During our discussion, we continue to refer to the new peak that appears in the olivine spectrum in the

253 800-900 cm-1 region as a "defect" feature, associated with the presence of highly coordinated SiO_6 or SiO_5

254 species formed by creating SiOSi linkages with adjacent SiO_4^{4-} units.

255 At the same pressure, broad background features also begin to appear underlying the sharp crystalline

256 peaks that are maintained in the spectra up to between 50-54 GPa (Fig. 1). Above 54 GPa the spectrum consists

257 entirely of these broad features that are typically interpreted as indicative of amorphous material. This is

258 maintained during decompression to ambient conditions (Fig. 1). The Raman spectrum of the recovered sample

259 differs substantially from that of olivine glass prepared by quenching from the melt at ambient pressure, that is

10

260   dominated by a strong band near 850 cm^{-1} due to the ν_1 symmetric stretching of isolated SiO_4^{4-} units (Piriou and

261   McMillan, 1983; Williams et al., 1989). Instead, the amorphous solid produced by PIA shows a broad band of

262   vibrational excitations at lower wavenumbers indicating the presence of highly coordinated silicate species. The

263   Raman spectrum of the high-density amorphous solid evolved slightly during decompression with development of

264   intensity in the 850-900 cm^{-1} range below 27 GPa, indicating the re-appearance of some proportion of tetrahedral

265   SiO_4 units within the structure. The vibrational density of states (VDOS) functions of simulated amorphous

266   Mg_2SiO_4 prepared by quenching from the liquid state in AIMD calculations at 0 and 59 GPa are compared in

267   Figure 4.

268   We continued with an investigation of powdered $(Mg_{0.88}Fe_{0.12})_2SiO_4$ olivine compressed using Ne as a

269   PTM to study the metastable transformation behavior under highly non-hydrostatic conditions (Fig. 5). The Raman

270   peaks exhibited additional broadening by 13.5 GPa due to deviatoric stresses generated within the pressed

271   powdered sample. However, as observed for the single crystal sample, a new 830 cm^{-1} "defect" peak appeared by

272   approximately 43.5 GPa. After allowing the sample to relax overnight, this peak increased in intensity, and a broad

273   amorphous background emerged underlying the crystalline features. The sample was not pressurized further so

274   that the crystalline peaks did not disappear. During decompression the characteristic Raman peaks of crystalline

275   olivine re-emerged immediately, although the defect feature was still observed down to 17 GPa. The position of

276   this peak extrapolated to ambient pressure indicated a value near 720 cm^{-1} (Fig. 3), close to that of the additional

277   defect feature noted previously in spectra of natural and laboratory shocked olivine samples (Heymann, 1990;

278   Heymann and Cellucci, 1988; Farrell-Turner *et al.*, 2005; Van de Moortèle *et al.*, 2007). Following complete

279   recovery to ambient conditions, the main features of the crystalline olivine spectrum reappeared but with different

280   relative intensities of the two main Si-O stretching peaks, and the remaining bands were broadened compared

281   with the starting material (Fig. 5).

282   We completed our study by compression and decompression of a hydrated sample prepared from San

283   Carlos olivine to investigate the effects of dissolved OH on the metastable transformations and their kinetics (Fig.

284   6). Upon raising the pressure between 31.5 and 47 GPa, the overall intensity of the Raman spectrum decreased

285   markedly, and the Si-O tetrahedral stretching features became broadened and less well resolved. The sample was

286   then left overnight at 47 GPa. A further reduction in overall Raman intensity was noted and broad amorphous

287   features along with the "defect" peak near 880 cm^{-1} appeared in the spectrum. Further compression to 50-54 GPa

288   led to further broadening and disappearance of the highest frequency Si-O stretching band in the 1000-1100 cm^{-1}

289   region. The Raman spectrum of this apparently amorphous OH-containing olivine sample was retained during

290   decompression, with re-appearance of broadened crystalline peaks below 3 GPa. The high frequency feature

291   resembled the tetrahedral SiO_4^{4-} stretching of olivine glass produced by melt quenching (Piriou and McMillan

292   1983; Williams et al. 1989). The appearance of this feature was detected in the Raman spectrum taken at 8 GPa

293   (Fig. 6). Following recovery to ambient conditions and leaving at 1 atm overnight, the crystalline olivine spectrum

294   re-emerged. It is obvious that the presence of OH groups within the olivine structure affects both the nature and

295   the kinetics of the metastable structural transformations, apparently favoring the retention of tetrahedrally bonded

296   species.

297

Discussion

299   Our results obtained during hydrostatic compression of a single crystalline San Carlos olivine sample composition

300   suggest that localized defect structures associated with formation of SiOSi linkages between previously

301   independent SiO_4^{4-} tetrahedra and associated with formation of 5- or 6-coordinated silicate species occur within

302   the structure above 41-42 GPa. Observation of the characteristic "defect" peak in the 800-900 cm^{-1} region that is

303   normally free from vibrational modes for olivine structures coincides with the appearance of broad background

304   features indicative of amorphous material. An initial conclusion would be that PIA has occurred with its onset near

305   41 GPa and completed by 54 GPa, accompanied by the formation of localized defects within the olivine structure,

306   that may have initiated the amorphization process.

307   Both our results and this interpretation differ from those of Finkelstein et al. (2014) who studied end-

308   member single crystalline Mg_2SiO_4 compressed hydrostatically in He under similar conditions to our experiment,

309   using single crystal X-ray structural refinement to follow structural changes in the material. Combining the X-ray

310   results with *ab initio* structure searching and metadynamics simulations they identified metastable crystalline

311   phase transitions occurring at 50 and 58 GPa into two new phases (Fo-II and Fo-III). They observed that the initial

312   olivine structure (Fo-I) was maintained metastably up to 48 GPa, with no indication of local defect formation or

313   amorphization. Above this pressure an abrupt transition occurred into the Fo-II phase at 50 GPa, quickly followed

314   by a second transition into the Fo-III phase upon further compression to 58 GPa. The *ab initio* searching and

315   metadynamics calculations confirmed the structures that were shown to contain interconnected SiO_4 and SiO_6

316   units, while intermediate SiO_5 species were also identified during the metastable structural transformation process

317   from olivine [Finkelstein et al., 2014].

318   Those observations lead to a possible alternative interpretation of our results. Our DFT calculations of the

319   Raman spectra of Fo-II using the structural parameters provided by Finkelstein et al. (2014) at 52.4 GPa show

320   they are dominated by strong peaks at 890 and 990 cm^{-1} at this pressure (Fig. 2). It might be possible that the

321   broadening and loss of resolution we observe in the high frequency SiO_4^{4-} stretching peaks along with the

322   appearance of the "defect" feature at 41.7 GPa could be associated with formation of domains of the Fo-II

323   structure within the natural single sample, at a lower pressure than that found by Finkelstein et al. (2014) due to

324   the presence of Fe^{2+} ions within the San Carlos olivine. The simultaneous appearance of broad background

325   scattering could then either be due to macroscopically amorphous domains produced within the sample due to the

326   kinetically hindered phase transformation and localized defects produced within the olivine structure, or might

327   instead indicate a mixture of the vibrational density of states (VDOS) from both Fo-I and Fo-II activated at the

328   Brillouin zone center by the presence of local defects and structural intergrowths that impede the propagation of

329   lattice vibrations. Our AIMD simulations demonstrate that the VDOS for metastably compressed Fo-I exhibits the

330   expected gap between SiO_4^{4-} deformation and tetrahedral stretching modes between 750-980 cm^{-1} at 44 GPa,

331   whereas the Fo-II vibrations extend throughout this region and up to 1320 cm^{-1} at around the same pressure (45

13

332 GPa) (Fig. 4). Our observation of the initial olivine "internal defect" formation coupled with the onset of PIA could in

333 fact reflect the occurrence of the metastable Fo-I to Fo-II phase transformation at significantly lower pressure (41

334 GPa vs 50 GPa) in the Fe^{2+}-containing natural sample.

335 In our study we observed complete amorphization occurring by 54 GPa for the olivine single crystal, with

336 broad amorphous Raman bands observed between 200-400 cm^{-1} and extending throughout the 500-900 cm^{-1}

337 region (Fig. 1). The Raman spectrum calculated by DFT for the Fo-III structure at 58.2 GPa shows a single strong

338 peak at 930 cm^{-1} (Fig. 2). However, the VDOS obtained from AIMD simulations of this phase shows a featureless

339 broad band extending between 100-1100 cm^{-1} at the same pressure (59 GPa), with perhaps a more prominent

340 feature developed near 670 cm^{-1} (Fig. 4). The VDOS for the high pressure crystal differs from the simulated

341 spectrum of a high-density Mg_2SiO_4 glass quenched from the liquid state at 59 GPa. Here there is an enhanced

342 contribution from the higher frequency Si-O stretching vibrations at higher wavenumber values due to the

343 presence of 4- and 5-coordinated silicate species. The average Si^{4+} coordination by O^{2-} ions is 5.14 compared with

344 3.96 for an Mg_2SiO_4 melt quenched at P = 0 GPa (Fig. 4). The low pressure quenched liquid exhibits an

345 enhanced intensity in the 900-1300 cm^{-1} region, with a clear separation from the lower frequency SiO_4^{4-}

346 deformation modes, and a prominent feature at 150-200 cm^{-1} due to Mg-O vibrations and SiO_4^{4-} librations.

347 During low temperature compression of crystalline samples into a highly metastable densified regime,

348 there is always a delicate balance between kinetic and thermodynamic factors determining structural changes and

349 phase transformations occurring in metastable phase space. In addition, the use of different methods to observe

350 and diagnose metastable crystalline transitions vs PIA can lead to different interpretations depending on the

351 characteristic length scale of the probe techniques used [Machon et al., 2014]. Because the structural

352 transformations are kinetically hindered they can result in different non-equilibrium pathways being followed, and

353 the resulting materials produced both at high pressure and recovered to ambient conditions an be different. In the

354 case of PIA investigations, the use of single crystals vs powdered samples, or the presence of compositional

355 impurities, as well as the nature and rate of compression conditions that can substantially affect the results and

356 their interpretations [Kingma et al., 1993; Ekbundit et al., 1996; Machon et al, 2014]. In addition, it is not always

14

357   easy to determine from experimental results such as X-ray diffraction or Raman scattering if defect formation or

358   PIA has occurred, or if the data reveal the presence of kinetically hindered metastable phase transitions involving

359   potentially locally disordered phases. These considerations are clearly revealed here by comparison of our results

360   with those of Finkelstein et al (2014).

361   The thermodynamic possibilities for these different cases occurring can be interpreted by considering the

362   free energy relations of metastably compressed phases [Machon et al., 2014]. Any crystal subject to a first order

363   transformation into a high density phase can be metastably compressed beyond its thermodynamic transition

364   pressure if the temperature is too low or the compression rate too rapid to initate and complete the expected

365   phase change. However, no system can be compressed indefinitely without undergoing a fundamental

366   mechanical, electronic or phonon instability resulting in structural collapse. If this collapse occurs at too low

367   temperature or on a too rapid timescale, ionic or atomic diffusion or bond rearrangements can not take place to

368   result in a new crystalline lattice and the result is an amorphous solid. Alternatively, the metastably compressed

369   crystal can undergo metastable phase transformations into new structural types as their free energy (G(P))

370   relations are intersected. Another event that can occur especially under non-hydrostatic pressurization conditions

371   is that the material leaves the metastable extension of its free energy G(P) curve at lower pressure but with

372   insufficient thermal energy to achieve the formation of metastable crystals, to result in a solid amorphous material.

373   Such a PIA process could have occurred during our metastable compression of $Fo_{90}Fa_{10}$ olivine under hydrostatic

374   conditions above 41 GPa, where the presence of Fe^{2+} substituting for Mg^{2+} ions might have lowered local

375   energetic barriers and thus affected the structural transformation kinetics.

376   The Raman signature of the dense amorphous solid produced by PIA and recovered following

377   decompression from single crystalline olivine following quasi-hydrostatic pressurization is notably different from

378   that of thermal $(Mg,Fe)_2SiO_4$ glasses formed by quenching from the liquid state [Pirou and McMillan, 1983;

379   Williams et al., 1989]. These glasses are dominated by a strong polarized peak near 850 cm^{-1} assigned to isolated

380   SiO_4^{4-} stretching vibrations that is absent here. The Raman spectrum observed following PIA at high pressure

381   clearly indicates a lower maximum in wavenumber values than the compressed orthosilicate crystal,

15

382 demonstrating the presence of higher coordinated (SiO_5 or SiO_6) units in the amorphous state. However, the

383 distribution of Raman peaks are also similar to the VDOS observed for the Fo-III crystalline material. The

384 amorphous spectrum evolved during decompression indicated the reappearance of tetrahedrally bonded silicate

385 units.

386 The formation of SiOSi linkages between adjacent SiO_4 tetrahedral units that results in the appearance of

387 SiO_5/SiO_6 species within metastably compressed olivine might represent an early stage in the crystalline

388 disordering leading to global PIA or to formation of Fo-II and Fo-III crystalline phases, occuring within the 40-45

389 GPa range at low temperature. Our studies also show that the defect formation and PIA processes continue to

390 progress if the sample is held at 43-45 GPa on laboratory timescales. In the case of our powdered samples

391 compressed non-hydrostatically to within this range an olivine phase is recovered but with evidence for nanoscale

392 structural reorganization and disordering within the crystalline domains, and the defect Raman signature is

393 retained down to low pressure (<17 GPa). During shock compression the amorphization and decompression

394 timescales are much shorter and this might result in the defect feature that has been recorded in Raman spectra

395 observed for naturally- and laboratory-shocked olivine samples (Farrell-Turner et al, 2005; Van de Moortèle et al,

396 2007).

397 Metastable compression of the OH-enriched olivine results in slightly different behavior indicating the

398 effects of incorporated OH groups on the kinetics of metastable local structure changes and crystalline

399 transformations. As for the "dry" samples, the $SiOSi/SiO_5$ defect feature is observed to appear above 42-43 GPa

400 along with first evidence for broad amorphous Raman scattering. However, unlike materials with low OH content,

401 the amorphous phase produced by 50 GPa still retains Si-O stretching vibrations that are diagnostic of isolated

402 SiO_4^{4-} species, presumably because of the presence of $SiO_3(OH)$ groups that hinder oligomerization of adjacent

403 silicate tetrahedra. However, by compression to 54 GPa, even these had mostly disappeared. During

404 decompression, the high pressure amorphous spectrum was maintained to below 29 GPa but a new feature

405 indicated the re-emergence of SiO_4^{4-} units within structural environments similar to olivine in the 800-900 cm^{-1}

16

406 region. As the pressure was reduced to 3 GPa the spectrum evolved to resemble that of olivine glass produced by

407 quenching from the liquid phase (Piriou and McMillan, 1983; Williams *et al.*, 1989), followed by re-appearance of

408 crystalline olivine peaks as the sample was recovered to ambient pressure conditions. The presence of OH groups

409 within the olivine structure thus affects the structural transformation kinetics and pathways, especially during

410 decompression. Previous studies have documented the effect of incorporated OH units in reducing the viscosity

411 of olivine and this is typically attributed to an enhancement of Si^{4+} diffusion within the crystal (Karato, 1986; Mei

412 and Kohlstedt 2000a, b). However, one recent investigation found no evidence for enhanced Si diffusion in the

413 presence of OH-bearing Mg_2SiO_4 forsterite, and even questioned the idea of significant hydrolytic weakening in

414 olivine (Fei et al., 2013). Our results demonstrate that the presence of minor amounts of OH do affect the kinetics

415 and transformation pathways of metastable structural and phase transitions in minerals at low temperatures where

416 enhanced ionic diffusion is unlikely to be implicated.

417

418 **Implications**

419   Our results have implications for the interpretation of natural and synthetic olivine materials recovered

420 following static and shock compression. Our diamond-anvil cell Raman results show that local defects and

421 amorphous structures can appear within olivine crystals subjected to hydrostatic and non-hydrostatic compression

422 at pressures lower than phase transitions found by single crystal and *ab initio* compression experiments that set

423 an upper limit for metastable crystal transformations under nearly equilibrium conditions. Laboratory shock and

424 natural impact events occurring at low temperatures may result in defect structures and dense diaplectic glass

425 retained within the olivine materials recovered and observed at ambient pressure. The diaplectic glass formed

426 during shock events at low temperature is likely to be based on highly coordinated silicate species, but these will

427 revert to tetrahedrally bonded orthosilicate glass structures if the glasses contain sufficiently high OH content.

428 Recrystallization is also expected to occur when polycrystalline materials are recovered following compression to

429 pressures above 40 GPa, and the "defect" peak indicating local formation of SiOSi linkages and SiO_5 species may

430 be lost. However locally non-isotropic strain fields developed and maintained within crystalline grains in shocked

17

431 meterorites can result in retention of such defect features in natural materials (Van de Moortele *et al.*, 2007). Our

432 data place new constraints on the interpretation of natural and laboratory shocked olivine samples in terms of the

433 P,T conditions to which they have been exposed.

434

435 **Acknowledgements**

438

439 **References Cited**

440 Aguado, A., Bernasconi, L., Jahn, S., and Madden, P.A. (2003) Multipoles and interaction potentials in ionic

441 materials from planewave-DFT calculations. Faraday Discussions, 124, 171-184.

442 Andrault, D., Bouhifd, M.A., Itie, J.P., and Richet, P. (1995) Compression and amorphization of $(Mg,Fe)_2SiO_4$

443 olivines: An x-ray diffraction study up to 70 GPa. Physics and Chemistry of Minerals 22, 99-107.

444 Birle, J.D., Gibbs, G.V., Moore, P.B., and Smith, J.V. (1968) Crystal structures of natural olivines. American

445 Mineralogist 53, 807-824.

446 Chopelas, A. (1990) Thermal properties of forsterite at mantle pressures derived from vibrational spectroscopy.

447 Physics and Chemistry of Minerals 17, 149-156.

448 Chopelas, A. (1991) Single-crystal Raman spectra of forsterite, fayalite and monticellite. American Mineralogist 76,

449 1101-1109.

450 Demouchy, S. and Mackwell, S. (2006) Mechanisms of hydrogen incorporation and diffusion in iron-bearing

451 olivine. Physics and Chemistry of Minerals, 33, 347-355.

452 Dovesi, R., Saunders, V.R., Roetti, C., Orlando, R., Zicovich-Wilson, C.M., Pascale, F., Civalleri, B., Doll, K.,

453 Harrison, N.M., Bush, I.J., D'Arco, Ph., Llunell, M., Causà, M., Noel, Y. (2014) CRYSTAL14 User's Manual,

454 University of Torino, Torino.

455 Durben, D.J., McMillan, P., and Wolf, G.H. (1993) Raman study of the high-pressure behavior of forsterite

456 Mg_2SiO_4 crystal and glass. American Mineralogist 78, 1143-1148.

457 Ekbundit, S., Leinenweber, K., Yarger, J.L., Robinson, J.S., Verhelst-Voorhees, M., and Wolf, G.H. (1996) New

458 high-pressure phase and pressure-induced amorphization of $Ca(OH)_2$: grain size effect. Journal of Solid State

459 Chemistry, 126, 300-307.

460 Farrell-Turner, S., Reimold, W.U., Nieuwoudt, M. and Erasmus, R.M. (2005) Raman spectroscopy of olivine in

461 dunite experimentally shocked to pressures between 5 and 59 GPa. Meteoritics & Planetary Science 40, 1311-

462 1327.

463 Fei, H., Wiedenbeck, M., Yamazaki, Daisuke and Katsura, T. (2013). Small effect of water on upper-mantle

464 rheology based on silicon self-diffusion coefficients. Nature, 498, 213-215.

465 Finkelstein, G.J., Dera, P.K., Jahn, S., Oganov, A.R., Holl, C.M., Meng, Y., and Duffy, T.S. (2014) Phase

466 transitions and equation of state of forsterite to 90 GPa from single-crystal X-ray diffraction and molecular

467 modelling. American Mineralogist, 99, 35-43.

468 Fournelle, J.H. (2011) An investigation of "San Carlos Olivine": comparing USNM-distributed material with

469 commercially available material. Microscopy and Microanalysis, 17 (Supplement 2), 842-843.

470 Ghose, S., Hastings, J.M., Choudhury, N., Chaplot, S.L., and Rao, K.R. (1991) Phonon dispersion relation in

471 fayaite, Fe_2SiO_4. Physica (B), 174, 83-86.

472 Gulyot, F. and Reynard, B. (1992) Pressure-induced structural modifications and amorphization in olivine

473 compounds. Chemical Geology, 96, 411-420.

474   Heymann, D. (1990) Raman study of olivines in 37 heavily and moderately shocked chondrites. Geochimica et

475   Cosmochimica Acta 54, 2507-2510.

476   Heymann, D. and Cellucci, T.A. (1988) Raman spectra of shocked minerals. 1-Olivine. Meteoritics, 23, 353-357.

477   Hofmeister, A.M. (1987) Single-crystal absorption and reflection spectroscopy of forsterite and fayalite. Physics

478   and Chemistry of Minerals, 14, 499-513.

479   Hofmeister, A.M. (1997) Infrared reflectance spectra of fayalite, and absorption data from assorted olivines,

480   including pressure and isotope effects. Physics and Chemistry of Minerals, 24, 535-546.

481   Hushur, A., Manghnani, M.H., Smyth, J.R., Nestola, F., and Frost, D.J. (2009) Crystal chemistry of hydrous

482   forsterite and its vibrational properties up to 41 GPa. American Mineralogist 94, 751-760.

483   Iishi, K. (1978) Lattice dynamics of forsterite. American Mineralogist, 63, 1198-1208.

484   Jahn, S. and Madden, P.A. (2007) Modelling Earth materials from crustal to lower mantle conditions: a

485   transferable set of interaction potentials for the CMAS system. Physics of the Earth and Planetary Interiors, 162,

486   129-139.

487   Jeanloz, R., Ahrens, T.J., Lally, J.S., Nord Jr., G.L., Christie, J.M., and Heuer, A.H. (1977) Shock-produced olivine

488   glass: First observation. Science, 197,457-459.

489   Jeanloz, R. (1980) Shock effects in olivine and the implications for Hugoniot data. Journal of Geophysical

490   Research, 85, 3163-3176.

491   Karato, S.I., Paterson, M.S. and Fitz Gerald,J.D. (1986) Rheology of synthetic olivine aggregates - influence of

492   grain-size and water. Journal of Geophysical Research, 91, 8151-8176.

493   Kerschhofer, L., Dupas, C., Liu, M., Sharp, T.G., Durham, W.B., and Rubie, D.C (1998) Polymorphic

494   transformations between olivine, wadsleyite and ringwoodite: mechanisms of intracrystalline nucleation and the

495   role of elastic strain. Mineralogical Magazine, 62, 617-638.

20

496   Kingma, K.J., Hemley, R.J., Mao, H.-k., and Veblen, D.R. (1993) New high-pressure transformation in α-quartz.

497   Physical Review Letters, 70, 3927-3930.

498   Klotz, S., Chervin, J.-C., Munsch, P., and Le Marchand, G. (2009) Hydrostatic limits of 11 pressure transmitting

499   media. Journal of Physics D: Applied Physics, 42, 075413.

500   Kohlstedt, D.L., Keppler, H. and Rubie, D.C (1996) Solubility of water in the α, β and γ phases of $(Mg,Fe)_2SiO_4$.

501   Contributions to Mineralogy and Petrology, 123, 345-357.

502   Kolesov, B. and Geiger, C. (2004) A Raman spectroscopic study of Fe-Mg olivines. Physics and Chemistry of

503   Minerals, 31, 142-154.

504   Machon, D., Meersman, F., Wilding, M.C., Wilson, M., and McMillan, P.F. (2014) Pressure-induced amorphization

505   and polyamorphism: Inorganic and biochemical systems. Progress in Materials Science 61, 216-282.

506   Manghnani, M.H., Hushur, A., Smyth, J.R., Nestola, F., Dera, P., Sekar, M., Amulele, G., and Frost, D.J. (2013)

507   Compressibility and structural stability of two variable hydrated olivine samples ($Fo_{97}Fa_3$) to 34 GPa by X-ray

508   diffraction and Raman spectroscopy. American Mineralogist 98, 1972-1979.

509   Mao, H.K. and Bell, P.M. (1972) Electrical conductivity and red shift of absorption in olivine and spinel at high

510   pressure. Science, 176, 403-406.

511   Maschio, L., Kirtman, B., Rérat, M., Orlando, R., Dovesi, R. (2013a) *Ab initio* analytical Raman intensities for

512   periodic systems through a coupled perturbed Hartree-Fock/Kohn-Sham method in an atomic orbital basis. I.

513   Theory. J. Chem. Phys. 139, 164101.

514   Maschio, L., Kirtman, B., Rérat, M., Orlando, R., Dovesi, R. (2013b) *Ab initio* analytical Raman intensities for

515   periodic systems through a coupled perturbed Hartree-Fock/Kohn-Sham method in an atomic orbital basis. II.

516   Validation and comparison with experiments. J. Chem. Phys. 139, 164102.

517   Mashimo, T., Kondo, K.I., Sawaoka, A., Syono, Y., Takei, H., and Ahrens, T.J. (1980) Electrical conductivity

518   measurement of fayalite under shock compression up to 56 GPa. Journal of Geophysical Research 85, 1876-

519   1881.

520   Mason, B. (1963) Olivine composition in chondrites. Geochimica et Cosmochimica Acta, 27, 1011-1023.

521   McMillan, P.F., and Akaogi, M. (1987) Raman spectra of β-Mg$_2$SiO$_4$ (modified spinel) and γ-Mg$_2$SiO$_4$ (spinel).

522   American Mineralogist 72, 361-364.

523   McMillan, P.F., Akaogi, M., Sato, R.K., Poe, B., and Foley, J. (1991) Hydroxyl groups in β-Mg$_2$SiO$_4$. American

524   Mineralogist 76, 354-360.

525   Mei, S and Kohlstedt, D.L. (2000a) Influence of water on plastic deformation of olivine aggregates 1. Diffusion

526   creep regime. Journal of Geophysical Research, 105, 21457-21469.

527   Mei, S and Kohlstedt, D.L. (2000b) Influence of water on plastic deformation of olivine aggregates 2. Dislocation

528   creep regime. Journal of Geophysical Research, 105, 21471-21481.

529   Noel, Y., Catti, M., D'Arco, Ph., and Dovesi, R. (2006) The vibrational frequencies of forsterite Mg$_2$SiO$_4$: an all-

530   electron ab initio study with the CRYSTAL code. Physics and Chemistry of Minerals, 33, 383-393.

531   Paques-Ledent, M.Th., and Tarte, P. (1973) Vibrational studies of olivine-type compounds-I. The IR and Raman

532   spectra of the isotopic species of Mg$_2$SiO$_4$. Spectrochimica Acta 29A, 1007-1016.

533   Piriou, B, and McMillan, P (1983) The high-frequency vibrational spectra of vitreous and crystalline orthosilicates.

534   American Mineralogist 68, 426-443.

535   Price, G.D., Parker, S.C., and Leslie, M. (1987) The lattice dynamics of forsterite. Mineralogical Magazine 51, 157-

536   170.

537   Prosandeev, S.A., Waghmare, U., Levin, I., and Msalar, J. (2005) First-order Raman spectra of $AB'_{1/2}B''_{1/2}O_3$

538   double perovskites. Physical Review B, 71, 214307.

539   Rao, K.R., Chaplot, S.L., Choudhury, N., Ghose, S., Hastings, J.M., Corliss, L.M., and Price, D.L. (1988) Lattice

540   dynamics and inelastic neutron scattering from forsterite, Mg_2SiO_4: Phonon dispersion relation, density of states

541   and specific heat. Physics and Chemistry of Minerals 16, 83-97.

542   Richard, G. and Richet, P. (1990) Room-temperature amorphization of faylaite and high-pressure properties of

543   Fe_2SiO_4 liquid. Geophysical Research Letters, 17, 2093-2096.

544   Ringwood, A.E. (1991) Phase transformations and their bearing on the constitution and dynamics of the mantle.

545   Geochimica et Cosmochimica Acta, 55, 2083-2110.

546   Servoin, J.L., and Piriou, B. (1973) Infrared reflectivity and Raman scattering of Mg_2SiO_4 single crystal. Physica

547   Status Solidi B 55, 677-686.

548   Schulien, S., Hornemann, U., and Stöffler, D. (1978) Geophysical Research Letters, 5, 345-348.

549   Sinogeikin, S.V., Katsura, T., and Bass, J.D. (1998) Sound velocities and elastic properties of Fe-bearing

550   wadsleyite and ringwoodite. Journal of Geophysical Research 103, 20819-20825.

551   Sinogeikin, S.V., Bass, J.D., and Katsura, T. (2003) Single-crystal elasticity of ringwoodite to high-pressures and

552   high-temperatures: Implications for 520 km seismic discontinuity. Physics of the Earth and Planetary Interiors 136,

553   41-66.

554   Soignard, E. and McMillan, P.F. (2004) Defect chemistry in γ-Si_3N_4 and γ-Ge_3N_4 spinel nitride phases probed by

555   Raman scattering in the laser-heated diamond anvil cell. Chemistry of Materials, 16, 3533-3542.

556   Sung, C.M., and Burns, R.G. (1976) Kinetics of the olivine-spinel transition: Inplication to deep-focus earthquakes

557   genesis. Earth and Planetary Science Letters 32, 165-170.

558   Van de Moortèle, B., Reynard, B., McMillan, P.F., Wilson, M., Beck, P., Gillet, P., and Jahn, S. (2007) Shock-

559   induced transformation of olivine to a new metastable $(Mg,Fe)_2SiO_4$ polymorph in Martian meteorites. Earth and

560   Planetary Science Letters 261, 469-475.

561   Wang, S.Y., Sharma, S.K., and Cooney, T.F. (1993) Micro-Raman and infrared spectral study of forsterite under

562   high pressure. American Mineralogist 78, 469-476.

563   Williams, Q., McMillan, P., and Cooney, T.F. (1989) Vibrational spectra of olivine composition glasses: The Mg-Mn

564   join. Physics and Chemistry of Minerals 16, 352-359.

565   Williams, Q., Knittle, E., Reichlin, R., Martin, S., and Jeanloz, R. (1990) Structural and electronic properties of

566   Fe_2SiO_4-fayalite at ultrahigh pressures: Amorphization and gap closure. Journal of Geophysical Research 95,

567   21549-21563.

568   Withers, A.C., Bureau, H., Raepsaet, C. and Hirschmann, M.M. (2012) Calibration of infrared spectroscopy by

569   elastic recoil detection analysis of H in synthetic olivine. Chemical Geology, 334, 92-98.

570   Yang, X., Liu, D. and Xia, Q. (2014) CO_2-induced small water solubility in olivine and implications for properties of

571   the shallow mantle. Earth and Planetary Science Letters, 403, 37-47.

572   Zha, C.S., Duffy, T.S., Downs, R.T., Mao, H.K., and Hemley, R.J. (1998) Brillouin scattering and x-ray diffraction of

573   San Carlos olivine: direct pressure determination to 32 GPa. Earth and Planetary Science Letters 159, 25-33.

574

575

576   **Figure captions**

577

578   **Figure 1.** Room temperature Raman scattering spectra of single-crystal San Carlos olivine during quasi-
579   hydrostatic compression in He at selected pressures up to 57 GPa on the upstroke and during decompression to 1
580   atm.

581

582   **Figure 2.** Raman spectra of Mg_2SiO_4 olivine caculated using first principles DFT methods up to 45.3 GPa along
583   with DFT calculations of spectra for Fo-II and Fo-III phases identified by Finkelstein et al. (2014) at 52.4 and 58.2
584   GPa respectively. The calculations were carried out using unit cell volumes corresponding to these pressures
585   indicated by the study of Finkelstein et al. (2014).

586

587   **Figure 3.** Pressure dependence of Raman active modes above 600 cm^{-1} for olivine samples. (a) The experimental
588   data for San Carlos $(Mg,Fe)_2SiO_4$ olivines include natural (solid symbols) and OH-enriched (empty symbols)
589   samples. The ν_2 SiO_4 bending vibration that shows an intensity increase above 31 GPa for all samples is seen to
590   maintain the same $d\nu/dP$ relation throughout the compression experiments. The new "defect" Raman mode that
591   appears above 40 GPa during compression of olivine samples is shown as starred symbols. Crossed stars
592   correspond to the peak retained to lower pressure during decompression for powdered San Carlos olivine. The
593    $(d\nu/dP)$ relation can be extrapolated to a frequency near 730 cm^{-1} at ambient pressure, corresponding to features
594   observed for naturally- and laboratory-shocked olivine samples. (b) Pressure dependence of Raman active modes
595   for Mg_2SiO_4 forsterite calculated using first principles DFT techniques.

596

597   **Figure 4.** Anisotropic ion molecular dynamics (AIMD) simulations of the vibrational density of states (VDOS, $g(\omega)$)
598   of Fo-I (a-Mg_2SiO_4) at 0 and 44 GPa, Fo-II at 45 GPa and Fo-III at 58 GPa, compared with simulated VDOS
599   spectra of amorphous Mg_2SiO_4 quenched from the simulated liquid state at 0 GPa and 59 GPa.
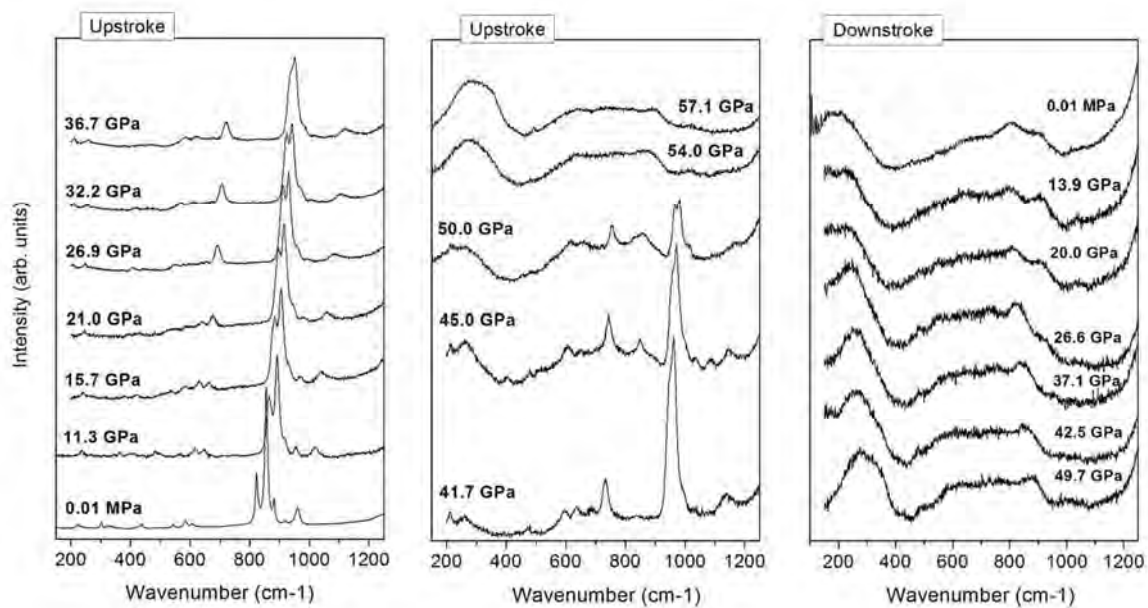
600

601   **Figure 5.** Room temperature Raman scattering spectra of San Carlos olivine powder at selected pressures up to
602   44 GPa.

603

604   **Figure 6.** Room temperature Raman scattering spectra of single-crystal OH-enriched San Carlos olivine powder at
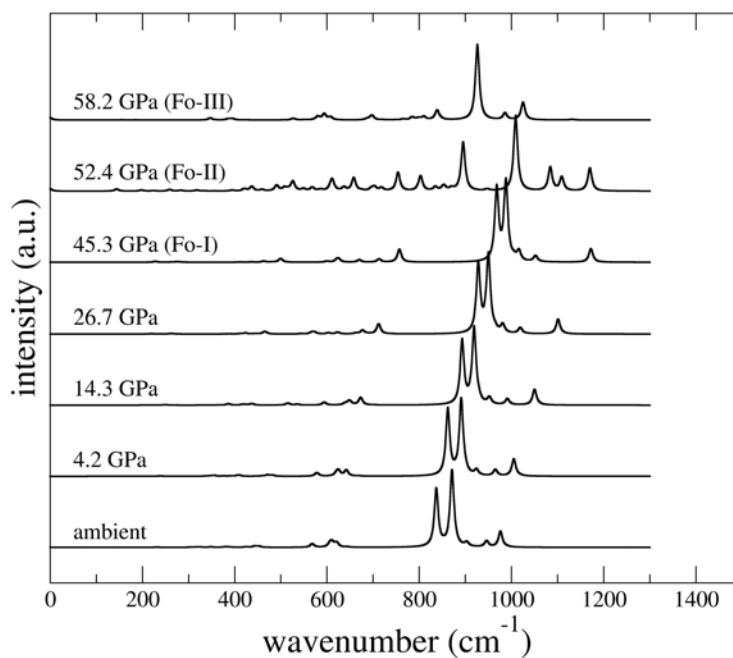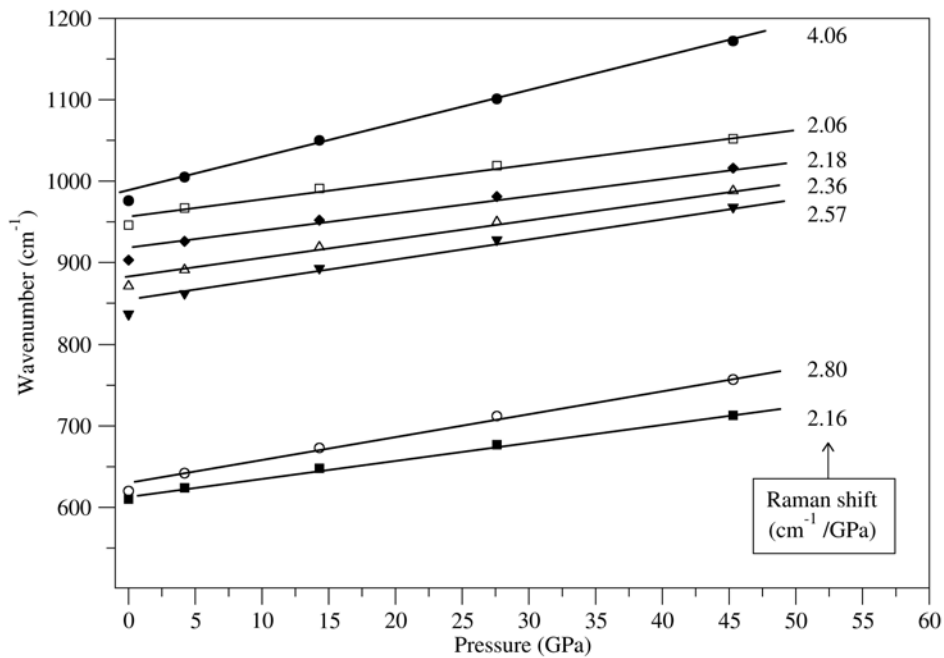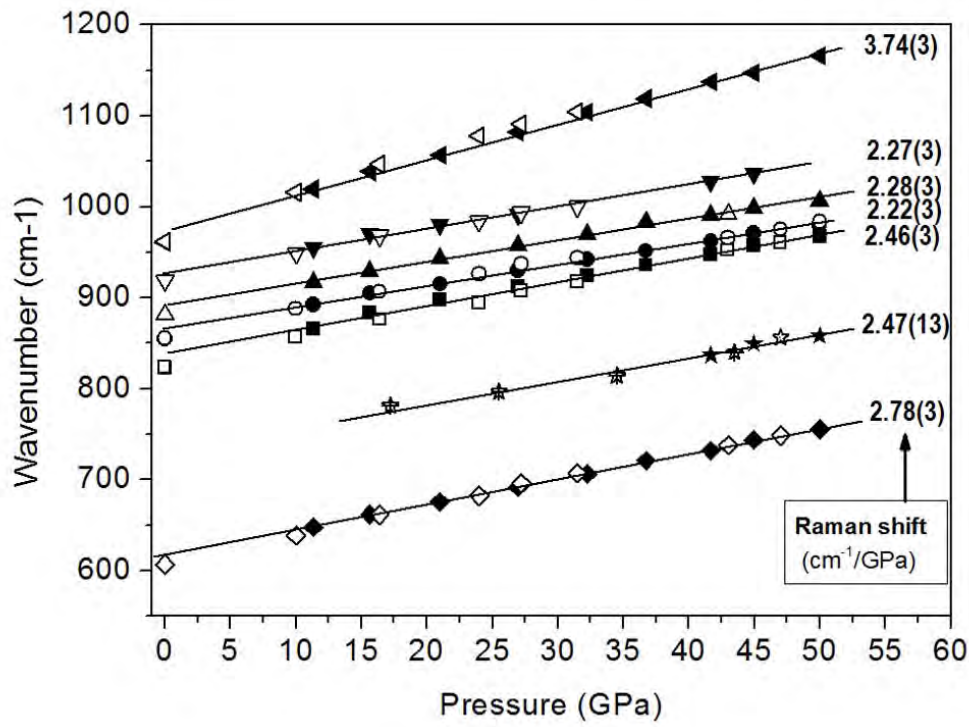605   selected pressures up to 54 GPa.

606

Figure 1

611

612

613 **Figure 2**

614

615

616

617   Figure 3

618

619

620

621

622   Figure 4

623
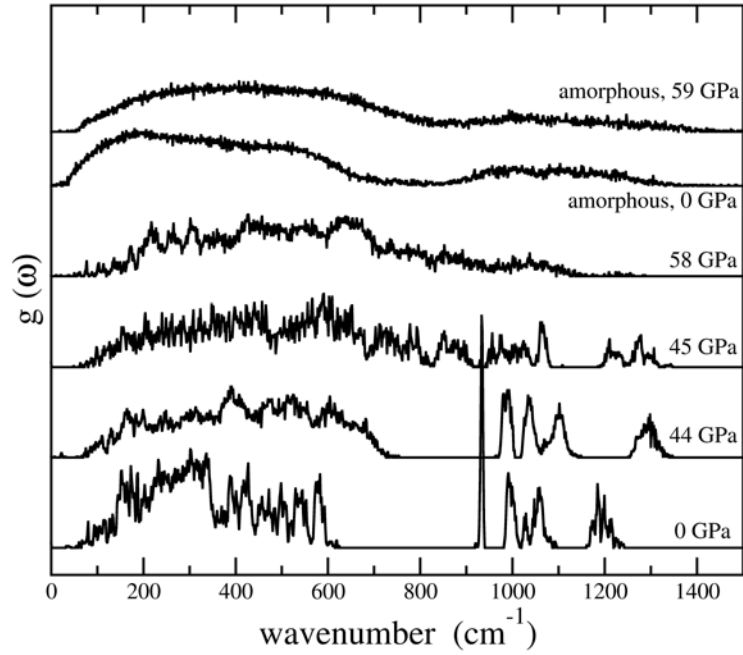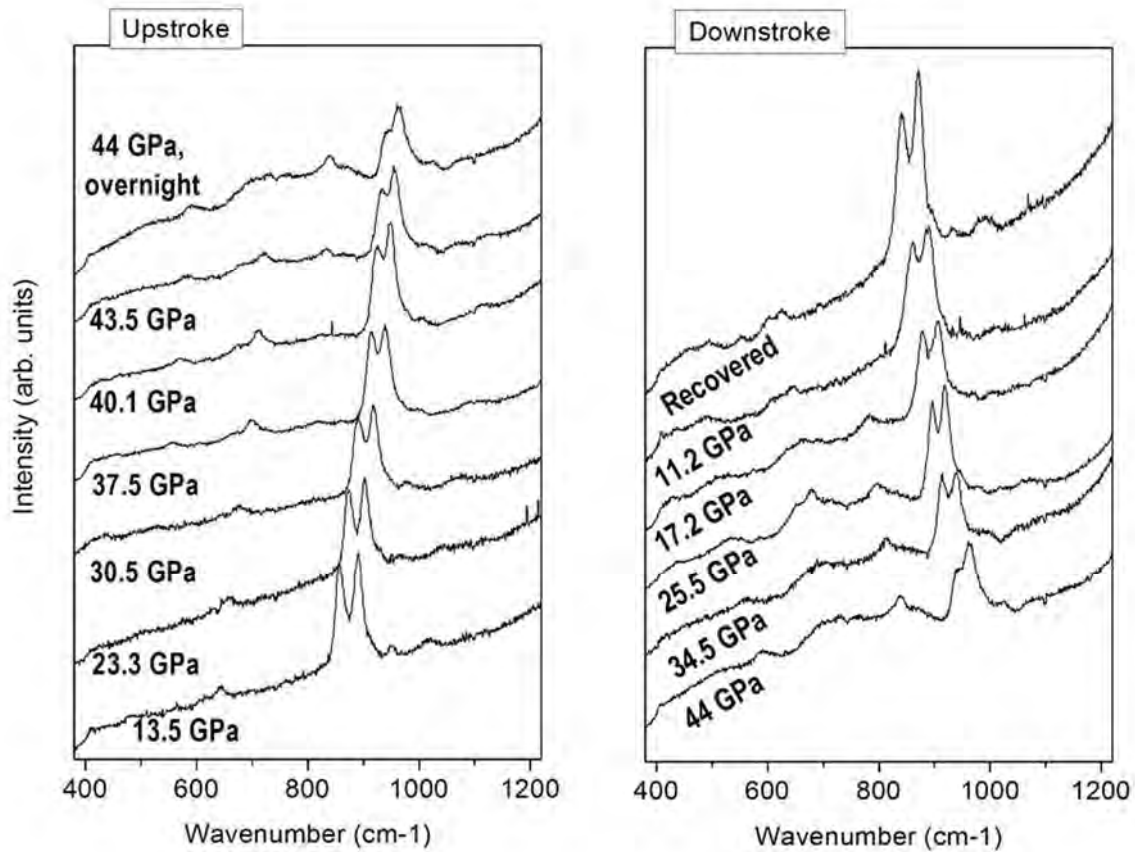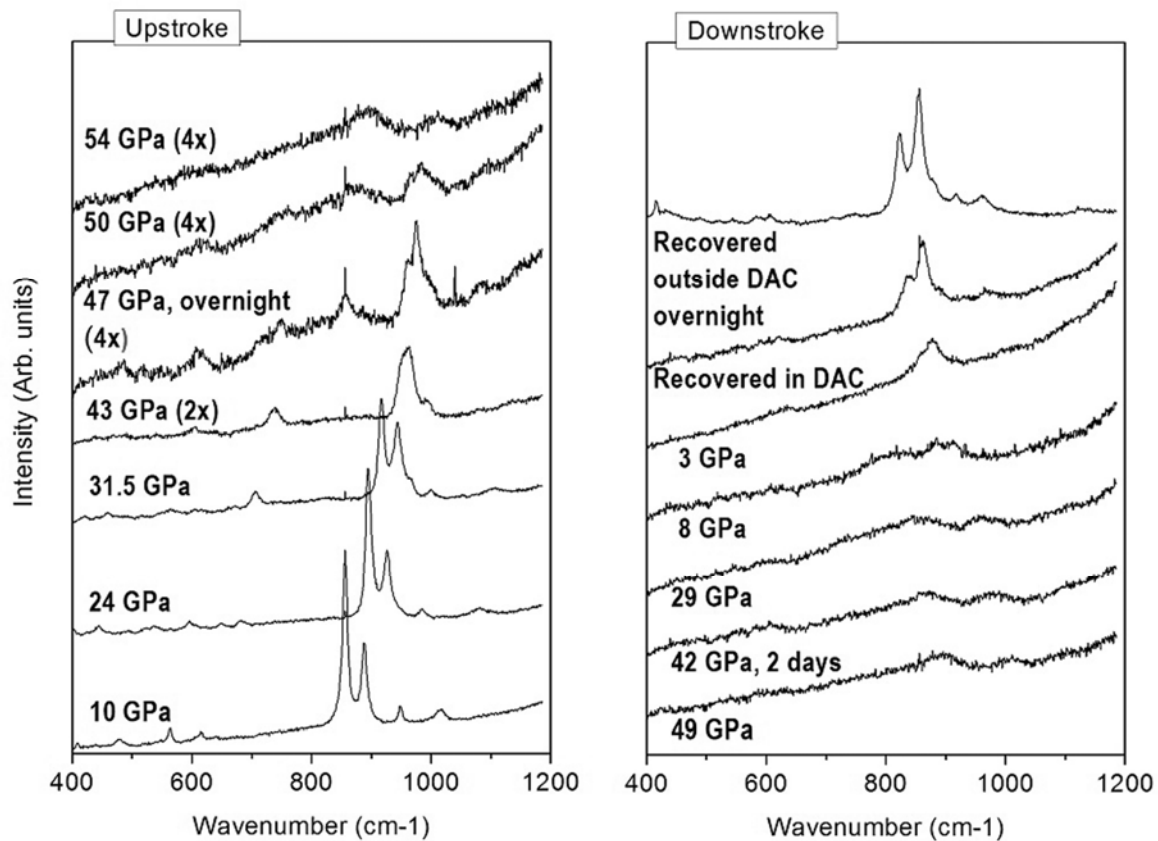
624

625

626   **Figure 5**

627

628

629

630

631

632 **Figure 6**

633

634